Composite Structures 246 (2020) 112394

Contents lists available at ScienceDirect

Composite Structures

journal homepage: www.elsevier.com/locate/compstruct

Geometrical modeling of tow wrinkles in automated fiber placement

Roudy Wehbe*, Brian Tatting, Sreehari Rajan, Ramy Harik, Michael Sutton, Zafer Gürdal

McNair Aerospace Center and Department of Mechanical Engineering, University of South Carolina, Columbia, SC 29201, USA

ARTICLE INFO

Keywords:
Automated fiber placement (AFP)
AFP defects
Wrinkling
Tow steering
Process modeling

ABSTRACT

This paper presents a thorough investigation of wrinkling within a path on a general surface for a composite tow constructed using the AFP process. Governing equations and assumptions for the presented model are derived based on geometrical considerations. A simple form of the wrinkled shape is assumed and applied to the inner edge of the tow path. For a given wavelength, the amplitude of the wrinkles can be approximated based on a worst-case scenario where all the difference in length between the edges of the path is absorbed through an out-of-plane wrinkle. The wrinkle wavelength can be obtained either from existing mechanics models in the literature or experimental measurements, otherwise an adequate wavelength can be assumed. A numerical solution is implemented to visualize wrinkles on the curved paths and to indicate potential regions for wrinkling on the surface. Several examples are presented to demonstrate the model, including constant angle paths on a double-curved surface and curved paths on a flat surface. From a geometrical standpoint, increasing the tow width or the path curvature results in an increase in the wrinkles' amplitude. Calculation of the wrinkles' amplitude for a steered path on flat surface shows good agreement with experimental measurements.

1. Introduction

Automated fiber placement (AFP) is a manufacturing process in which a numerically controlled robot or gantry system delivers strips of composite materials at a specific position and orientation through a machine head. A single strip of this material is named tow or a slit-tape, with a typical width of 3.175 mm up to 25.4 mm (⅛ in up to 1 in) [1]. Normally AFP delivers multiple adjacent tows to form a course, while a sequence of courses is termed ply, and a stack of multiple plies forms a laminate/composite part. During the manufacturing process, tows coming from spools and tensioners are fed through the machine head to the compaction roller where heat and pressure is applied for the material to adhere to the surface (Fig. 1). Another advantage of the AFP process is the ability to control differential feeding of the tows thus making it possible to lay material over complex surfaces and allow steering.

Due to the complexity of the AFP mechanism, the material being used, or the part geometry to be manufactured, several defects may arise during the manufacturing process and can be detrimental to the quality of the produced part. Some of these defects can be related to the material variability, some to the machine or process parameters and others to the design or geometrical model itself. Typical defects observed during the manufacturing process are gaps/overlaps, wrinkles (Fig. 2), tow twists, folds, spliced tows, and others [4,5]. The presence of these defects during manufacturing is usually undesirable, and in most cases, the process is interrupted for manual inspection and repairs, which leads to a decrease in the productivity. Recent automated inspection techniques are pushing towards complete characterization of defects in order to reduce the time-consuming visual inspection [6]. However, having the capability to detect these defects in the design phase, especially wrinkling, can lead to a substantial improvement in the manufacturing process. This requires a good understanding of the part geometry, the layup strategies used in the AFP process [7], and the influence of the AFP process parameters on the tow deformations.

Wrinkling, which is the subject of the present study, is a very broad term and can occur in several physical aspects such as human skin [8], fabric or clothing items [9], flowers and leaves due to excessive growth [10]. A general theory for wrinkling is presented in [11] based on the balance between the bending energy and the stretching energy of the thin film on a substrate. This theory can be extended to cover several physical problems using a scaling law, in which the wavelength of the wrinkles λ is proportional to $K^{-1/4}$ with K being the stiffness of the elastic substrate, and the amplitude of the wrinkles is proportional to the wavelength λ [11]. Another model for wrinkling applied to footwear design is presented in [12], where 2 shape operators that generates wrinkles are described based on the surface properties and optimized for minimum material usage. Wrinkling during manufacturing of composite structure has been discussed in the literature for several

* Corresponding author.
E-mail address: rwehbe@email.sc.edu (R. Wehbe).

https://doi.org/10.1016/j.compstruct.2020.112394
Received 22 January 2020; Received in revised form 9 April 2020; Accepted 16 April 2020
Available online 25 April 2020

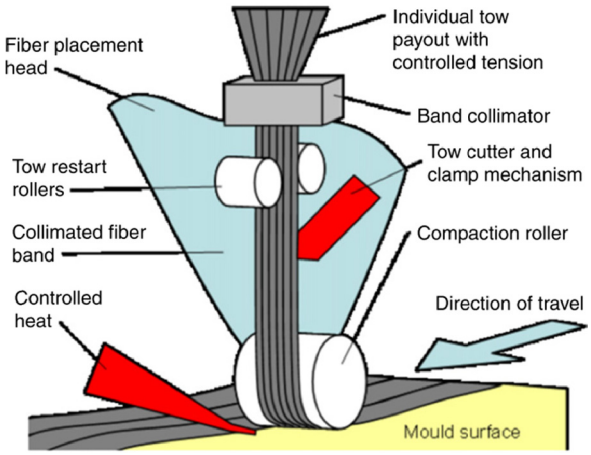

Fig. 1. Automated fiber placement head [2].

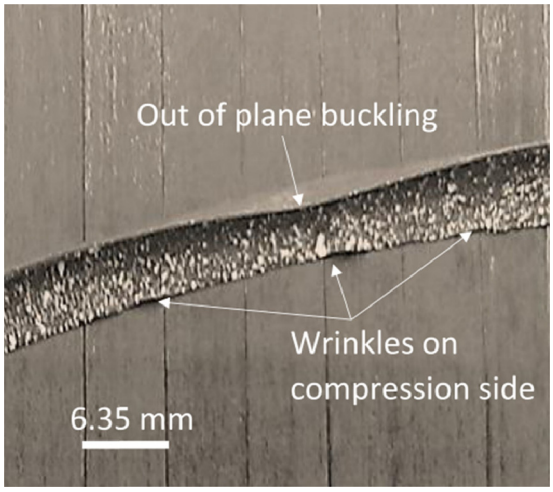

Fig. 2. Buckled tow in a laminate with steered fiber courses [3].

processes, such as diaphragm forming [10], draping (hand layup) [16], consolidation of prepreg over an external [12] and internal [13] radius, or due to shear between the prepreg and the mold [15]. The common reason behind such defect is the mismatch in dimension between the material and the mold surface.

In the context of AFP, wrinkling or sometimes referred to as puckering, or tow buckling is the out-of-plane deformation of the compressive edge of the tow that resembles wavy patterns (Fig. 2). Tow wrinkling during AFP is mainly observed while excessively steering the fiber tows to follow curvilinear paths on flat surfaces or non-geodesic paths on general surfaces. The primary reason for wrinkling occurrence is the mismatch in length between the prescribed path on the surface and the actual length of the tow delivered from the machine head. To absorb these differential lengths caused by the length mismatch, six deformation mechanisms are suggested in [13] that are shown in Fig. 3. These mechanisms can be classified under three categories: (I) elastic deformations, (II) in-plane deformations, and (III) out-of-plane deformations. Depending on the material properties of the tow and the adhesion level to the substrate, the fiber bundles within the tow can deform following one or more of the suggested mechanisms [14,15]. Usually, the large out-of-plane deformation are considered as concerning defects during the process.

Regarding wrinkling of carbon fiber tows during steering using AFP, the research efforts in the literature can be classified under two categories: experimental trials to determine a defect free layup based on a set of processing parameters [16–19], and mechanics models relating the material properties and tow geometry to a critical steering radius [20–23]. During experimental investigations, the processing parameters such as the layup speed, temperature and compaction pressure are varied for a given steering radius while observing the quality of the layup and the obtained defects. Varying the process parameters can alter the material property of the tow locally especially the tackiness between the tow and the substrate, hence possibly changing the tow deformation mechanisms (Fig. 3). In the mechanics models, a local approach is used where the wrinkles form individually along the length of the tow. The first model presented in [20] considers the wrinkling formation as a buckling problem of an elastic orthotropic plate laying on an elastic foundation representing tackiness. This model has been improved successively in the literature by first adjusting the boundary conditions in [21], adding a shear layer to better approximate the tackiness in [22], and most recently, considering the time-dependent behavior of the viscoelastic foundation in [23].

In this paper, a global approach is considered for the development of governing equations for wrinkling analysis of AFP tows. Given a tow-path or a layup over a surface, wrinkling patterns are generated for a given wavelength. The amplitude of the wrinkles can therefore be approximated based on a worst-case scenario where all the difference in length between the edges of the path is absorbed through an out-of-plane wrinkle when the tow separates from the surface and a wrinkle forms on the shorter edge. The wrinkle wavelength can be obtained either from existing mechanics models in the literature or experimental measurements, otherwise an adequate wavelength can be assumed. Using this approach, critical locations for wrinkle formation along with their corresponding sizes can be determined for a given path or layup, thus allowing further optimization of the processing parameters in future steps. In Section 2, the governing equations and geometrical parameters for the wrinkling analysis on general and flat surfaces are presented. Test cases of the model are shown in Section 3 for an unspecified material system where the wrinkle wavelength is assumed. In Section 4, the model is applied to a thermoset tow where the wrinkle wavelength is obtained from mechanics models and experimental measurements. Finally, conclusions and future work are presented in Section 5.

2. Tow-path modeling on general surfaces

This section presents the relevant geometrical parameters and governing equations for wrinkling analysis on a general surface. Those parameters are the tool surface and its corresponding tangent and normal vectors, the relevant path on the surface, its tangent, normal and bi-normal vectors, the tow surface and its geodesic curvatures. Concerning assumptions regarding the assumed shape function of the wrinkles and computation of parallel curves on the surface are presented. The wrinkling model applied to the general surface is further reduced for the simple case of a flat surface where relevant simplified equations are shown.

2.1. Surface modeling

A general three-dimensional surface is represented through surface parameters (u, v) such that:

$$\boldsymbol{S}(u,v) = X(u,v)\hat{i} + Y(u,v)\hat{j} + Z(u,v)\hat{k} \tag{1}$$

where the coefficient functions (X, Y, Z) are defined for each unit vector in three-dimensional Cartesian coordinates. Once the surface is defined, an orthonormal frame on that surface can be defined using the two tangent vectors and the normal vector in the $u$and v directions. The normalized tangent vectors along the surface parameters $u$and v are denoted by $\widehat{\boldsymbol{S}_u}$ and $\widehat{\boldsymbol{S}_v}$, and are given by:

$$\widehat{\boldsymbol{S}_u}(u,v) = \frac{\partial \boldsymbol{S}(u,v)/\partial u}{\|\partial \boldsymbol{S}(u,v)/\partial u\|}, \quad \widehat{\boldsymbol{S}_v}(u,v) = \frac{\partial \boldsymbol{S}(u,v)/\partial v}{\|\partial \boldsymbol{S}(u,v)/\partial v\|}, \tag{2}$$

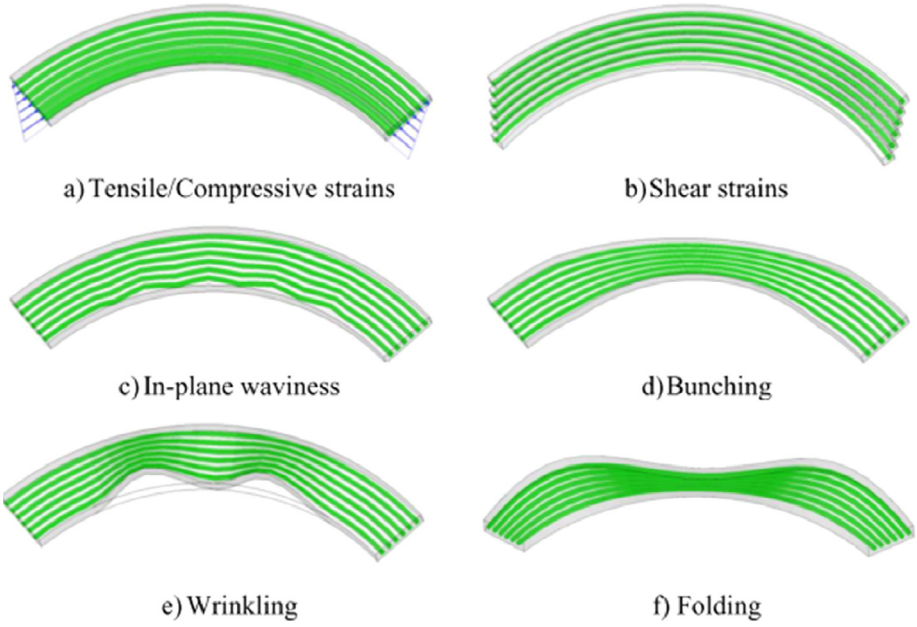

Fig. 3. Deformation mechanisms for differential length absorption [13].

where the subscripts represent differentiation with respect to those variables, the operator $\|\bullet\|$ denotes the Euclidean norm and the hat symbol ^ signifies a unit vector. The unit normal vector to the surface is defined as the cross product between the surface tangents and represents the third vector of the orthonormal frame for a surface:

$$\hat{\boldsymbol{N}}(u, v) = \frac{\boldsymbol{S_u} \times \boldsymbol{S_v}}{\|\boldsymbol{S_u} \times \boldsymbol{S_v}\|} \text{ or } \hat{\boldsymbol{N}}(u, v) = \hat{\boldsymbol{S_u}} \times \hat{\boldsymbol{S_v}}. \tag{3}$$

Infinitesimal distance between two points $\boldsymbol{P}(u, v)$ and $\boldsymbol{P}(u + \Delta u, v + \Delta v)$ on the surface is given by:

$$ds^2 = Edu^2 + Fdudv + Gdv^2, \tag{4}$$

where the scalar quantities E, F and G are the coefficients of the first fundamental form relative to the surface $\boldsymbol{S}(u, v)$and given by:

$$E(u, v) = \boldsymbol{S_u} \bullet \boldsymbol{S_u}, \quad F(u, v) = \boldsymbol{S_u} \bullet \boldsymbol{S_v}, \quad G(u, v) = \boldsymbol{S_v} \bullet \boldsymbol{S_v}, \tag{5}$$

where the symbol "•" denotes the dot product.

2.2. Path definition

The previous section defined an arbitrary surface on which the fiber tows have to be laid. An infinite number of possibilities exist for the definition of a fiber path over a general 3D surface. The most common approach used for parts produced by AFP is to take constant angle paths relative to the parts' major axis. These angles are typically $\pm 45^{\circ}$, 0°, and 90°, which are typically used in commercial parts. Other types of fiber path used in the literature can be classified under variable angle paths [7] such as geodesics, constant curvature paths [24], and curves with linear [25] and nonlinear angle variation [26]. For more details on fiber path planning for AFP, readers can refer to reference [7]. In the scope of this section only the derivation of a geodesic path will be presented since it has direct relevance to the solution process, though the formulation allows for any arbitrary definition of a path. For the definitions of the surface and path Fig. 4 is used as a reference.

An arbitrary path on the surface can be defined by:

$$\boldsymbol{C}(t) = \boldsymbol{S}(u_c(t), v_c(t)), \tag{6}$$

where t is an arbitrary parameter for the domain of definition, $u_c(t), v_c(t) \in \Omega$, of the surface. A very important feature in analyzing the path is the distance (arc length) along the path. The distance d between two points on the surface along the curve

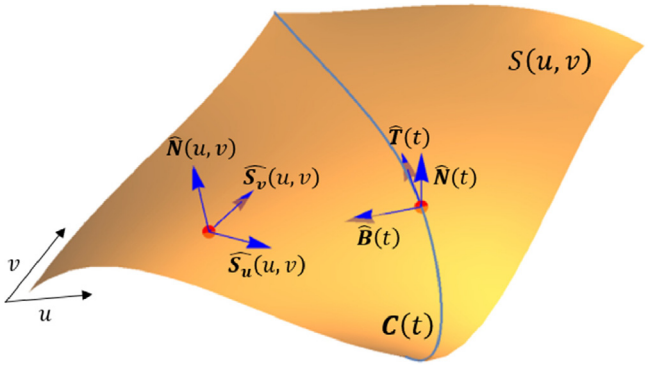

Fig. 4. Surface and path definition.

$\boldsymbol{C}(t) = \boldsymbol{S}(u_c(t), v_c(t))$ can be found through integration along the path of the distance between two points on a surface from equation (4):

$$d = \int_{t_a}^{t_b} \sqrt{E\left(\frac{du_c}{dt}\right)^2 + F\frac{du_c}{dt}\frac{dv_c}{dt} + G\left(\frac{dv_c}{dt}\right)^2}\, dt. \tag{7}$$

Using the length calculation along the curve, a re-parametrization of the path $\boldsymbol{C}(s)$ can be made as a function of the arclength s, where for a given length s_0 the location on the path $\boldsymbol{C}(s_0)$ can be determined, which is useful for the wrinkle shape function described in the later section.

In the analysis of a path along the surface, an additional useful orthonormal frame is defined using the following three vectors: $\hat{\boldsymbol{T}}$ the unit tangent to the path, $\hat{\boldsymbol{N}}$ the unit normal to the surface along the path, and $\hat{\boldsymbol{B}}$ the unit in-plane normal. This last vector $\hat{\boldsymbol{B}}$ (often referred to as the bi-normal or bi-tangent in the literature) is tangent to the surface at a given point but orthogonal to the tangent vector along the curve. It is represented through a cross-product of the normal and tangent vectors. These three vectors are expressed as:

$$\hat{\boldsymbol{T}}(t) = \frac{d\boldsymbol{C}(t)/dt}{\|d\boldsymbol{C}(t)/dt\|} = \frac{\boldsymbol{S_u}du_c/dt + \boldsymbol{S_v}dv_c/dt}{\|\boldsymbol{S_u}du_c/dt + \boldsymbol{S_v}dv_c/dt\|}, \tag{8}$$

$$\hat{\boldsymbol{N}}(t) = \hat{\boldsymbol{N}}(u_c(t), v_c(t)), \tag{9}$$

$$\hat{\boldsymbol{B}}(t) = \hat{\boldsymbol{N}}(t) \times \hat{\boldsymbol{T}}(t). \tag{10}$$

2.3. Geodesic path definition and geodesic curvature

A geodesic path on a surface is the shortest path connecting two points on that surface. A geodesic path can be defined starting at a point with a given direction of travel. The equations governing the path of a geodesic arise from minimization of the integral in equation (7) with appropriate boundary conditions, and for a general surface is calculated numerically. A geodesic path has to satisfy the following system of differential equations [27]:

$$\begin{cases} u'' + \Gamma^1_{11}u'^2 + 2\Gamma^1_{12}u'v' + \Gamma^1_{22}v'^2 = 0 \\ v'' + \Gamma^2_{11}u'^2 + 2\Gamma^2_{12}u'v' + \Gamma^2_{22}v'^2 = 0 \end{cases}, \tag{11}$$

where primes ($'$) represent differentiation with respect to the parameter t and Γ^i_{jk} are the Christoffel symbols of the surface $\boldsymbol{S}$ given in the appendix. To solve this system of second order differential equations, four initial conditions must be prescribed. In the following sections, a starting point with a prescribed direction are used to solve the geodesic equation to compute the parallel paths on the surface.

Lastly, several specific measures of curvature can be defined for the geometric formulation that has been discussed. The most important estimate of curvature for the problem under consideration is referred to here as the geodesic curvature k_g, which measures the curvature within the tangent plane for a curve on a surface. This parameter depends on both the surface parameters and the path definition and provides a direct indication on where wrinkles might form for tow-paths. It is calculated as [27]:

$$k_g = [(u_c'' + \Gamma^1_{11}u_c'^2 + 2\Gamma^1_{12}u_c'v_c' + \Gamma^1_{22}v_c'^2)v_c' - (v_c'' + \Gamma^2_{11}u_c'^2 + 2\Gamma^2_{12}u_c'v_c' + \Gamma^2_{22}v_c'^2)u_c'] \times \frac{\sqrt{EG - F^2}}{(Eu_c'^2 + 2Fu_c'v_c' + Gv_c'^2)^{\frac{3}{2}}}. \tag{12}$$

Note that for a geodesic curve that satisfies equation (11) the geodesic curvature is identically zero, which affirms that the geodesic is the "straightest" path on a surface.

2.4. Parallel curves on the surface and tow surface

For a given base curve (reference curve) on the surface, parallel paths (see Fig. 5) on one or both sides of the base curve have to be defined in order to determine the area covered by a carbon fiber tow. In addition, parallel curves can be used to generate the centerlines and the edges of adjacent tows, in the case if more than one tow is fed during a single course. Several algorithms to find parallel curves on general surfaces exist in the literature, such as projection techniques [28], orthogonal plane-surface intersection [29,30], geodesic offset [31], and others. In this paper, the algorithm used to compute parallel curves is similar to the one presented in [31], and is summarized as follows:

- Take n points $\boldsymbol{P_i}$ along the base curve: $\boldsymbol{P_i} = \{\boldsymbol{P}_1, \boldsymbol{P}_2, \cdots, \boldsymbol{P_n}\}$, $i = 1 \cdots n$
- Find each geodesic $\boldsymbol{G_i}$ starting at $\boldsymbol{P_i}$ in the direction orthogonal to the base curve
- Find the points $\boldsymbol{Q_i}$ on the geodesics at a distance d_i equal to the tow width or half-tow width, depending on the application
- Generate the parallel path $\boldsymbol{C_p}(s)$ by interpolating the points $\boldsymbol{Q_i}$ in the u-v space
- Map the parallel path from the u-v space to the cartesian space using $\boldsymbol{S}$

From these parallel path curve calculations, their lengths on the surface and geodesic curvatures can be computed from equations (7) and (12), respectively. Note that for the case where the base curve is parameterized by its arclength $\boldsymbol{C}(s)$, the obtained parallel curve $\boldsymbol{C_p}(s)$ has a different length due to the curvature (which drives the wrinkling problem), and the arclength parameter s does not reflect the length of the parallel curve anymore.

The surface that should be covered by a tow is bounded by the initial path $\boldsymbol{C}(s)$ and the interpolated parallel curve $\boldsymbol{C_p}(s)$. The equation of the tow surface can be generated by first creating a ruled surface $\boldsymbol{S_{tow,(u,v)}}(s, n)$ in the (u, v) domain, where $n = 0$ corresponds to the initial reference path $\{u_c(s), v_c(s)\}$ and $n = 1$ corresponds to the parallel path $\{u_p(s), v_p(s)\}$:

$$\boldsymbol{S_{tow,(u,v)}}(s, n) = \begin{Bmatrix} u_{tow}(s, n) \\ v_{tow}(s, n) \end{Bmatrix} = (1 - n)\begin{Bmatrix} u_c(s) \\ v_c(s) \end{Bmatrix} + n\begin{Bmatrix} u_p(s) \\ v_p(s) \end{Bmatrix}. \tag{13}$$

Then, the actual surface of the tow on the mold is generated by mapping $\boldsymbol{S_{tow,(u,v)}}(s, n)$ from (u, v) domain to the physical domain by:

$$\boldsymbol{S_{tow}}(s, n) = \boldsymbol{S}(u_{tow}(s, n), v_{tow}(s, n)). \tag{14}$$

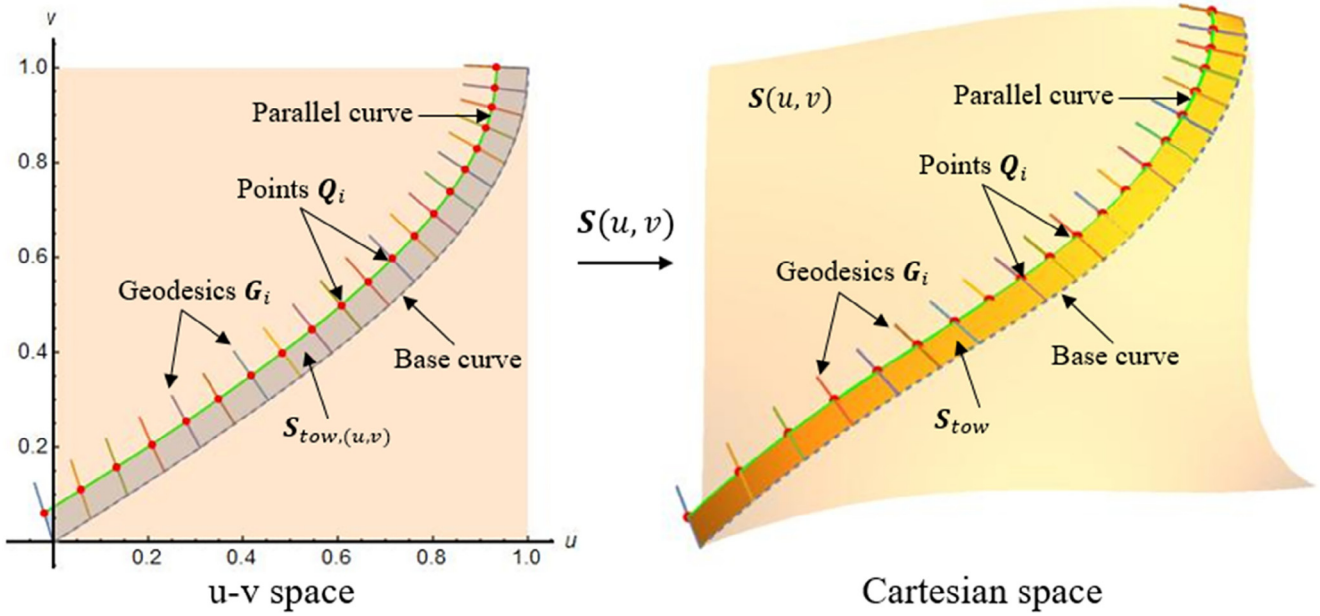

Fig. 5. Parallel curves computation on the surface.

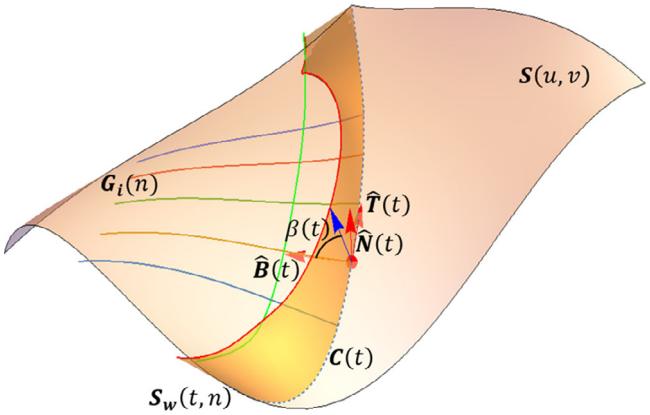

Fig. 6. Schematic of a wrinkle on a general surface.

2.5. Modeling assumptions for wrinkled tow

The previous sections provided the necessary equations to calculate lengths and curvatures of prescribed paths and their parallel curves on a general surface. For paths on general surfaces, the relative lengths of the inner and outer edges of a tow-path with a finite width are usually different. The AFP hardware on the other hand dispenses tows that have equal length on both edges. The differential length on the part surface between the two edges of the tow has to be somehow absorbed through a deformation mechanism (Fig. 3) within the tow to take the excess length on one edge of the tow that has to fit onto the part surface. Here it is assumed that the edge of the tow separates from the shorter edge on the surface while the tow's edge corresponding to the longer edge on the surface remains on its prescribed path. This will generate out-of-plane wrinkles along the length of the tow (refer to schematic in Fig. 6). To summarize, the following assumptions are therefore considered for the geometric modeling of the wrinkles:

1. The longest edge of the tow-path will remain on the surface of the tool after placement.
2. The shortest edge of the tow-path will totally lift from the surface to form the wrinkle.
3. The wrinkling formation is approximated by the rotation of the shortest edge around the longest.
4. The rotation angle is assumed to be a cosine function so that the shape of the obtained wrinkle is similar to the buckling of a plate with clamped-end conditions.
5. The shape of the buckled tow in the transverse direction will remain the same as the tow surface $\boldsymbol{S_{tow}}(s, n)$ before buckling (linear for the case of a flat plate, higher order for general surfaces).

Based on these assumptions, and assuming that the reference path is longer than the parallel path, the wrinkled surface of the tow $\boldsymbol{S_w}(s, n)$ (Fig. 6) is derived from the tow surface $\boldsymbol{S_{tow}}(s, n)$ in the following equation:

$$\boldsymbol{S_w}(s, n) = \boldsymbol{S_{tow}}(s, 0) + (\boldsymbol{S_{tow}}(s, n) - \boldsymbol{S_{tow}}(s, 0)) \bullet \mathscr{R}(\hat{\boldsymbol{T}}(s), \beta(s)), \quad (15)$$

where $\mathscr{R}(\hat{\boldsymbol{T}}(s), \beta(s))$ is Rodrigues' rotation matrix corresponding to the rotation by an angle $\beta(s)$ about the axis $\hat{\boldsymbol{T}}(s)$, the unit tangent to the original path. The first term in equation (15), $\boldsymbol{S_{tow}}(s, 0)$, corresponds to the reference path and represents the 1st assumption concerning the longest edge remaining on the surface. For the case where the parallel path is the longest, the $\boldsymbol{S_{tow}}(s, 0)$ terms in equation (15) should be replaced by $\boldsymbol{S_{tow}}(s, 1)$. The second term in equation (15) represents the shape of the wrinkled tow in the transverse direction n at each locations. This shape remains unchanged as stated in assumption #5. Rodrigues' rotation matrix $\mathscr{R}(\hat{\boldsymbol{T}}, \beta)$ computes the rotation by the angle β about the unit axis $\hat{\boldsymbol{T}} = \{\hat{T}_x, \hat{T}_y, \hat{T}_z\}$ and can be represented in matrix form as follows [32]:

$$\mathscr{R}(\hat{\boldsymbol{T}}, \beta) = \begin{pmatrix} \cos\beta + \hat{T}_x^2(1-\cos\beta) & -\hat{T}_z\sin\beta + \hat{T}_x\hat{T}_y(1-\cos\beta) & \hat{T}_y\sin\beta + \hat{T}_x\hat{T}_z(1-\cos\beta) \\ \hat{T}_z\sin\beta + \hat{T}_x\hat{T}_y(1-\cos\beta) & \cos\beta + \hat{T}_y^2(1-\cos\beta) & -\hat{T}_x\sin\beta + \hat{T}_y\hat{T}_z(1-\cos\beta) \\ -\hat{T}_y\sin\beta + \hat{T}_x\hat{T}_z(1-\cos\beta) & \hat{T}_x\sin\beta + \hat{T}_y\hat{T}_z(1-\cos\beta) & \cos\beta + \hat{T}_z^2(1-\cos\beta) \end{pmatrix}. \quad (16)$$

One of Rodrigues' rotation's conditions is that the rotation axis should pass through the origin of the reference system. Hence the third term in equation (15) ensures this condition by applying the necessary translation of "$-\boldsymbol{S_{tow}}(s, 0)$". Also, by choosing the rotation axis to be the unit tangent vector $\hat{\boldsymbol{T}}(s)$, assumptions 1, 2, and 3 are satisfied. Lastly, the remaining term in equation (15) is the rotation angle $\beta(s)$. This angle is assumed to have a cosine shape function as stated in assumption #4, and is given by:

$$\beta(s) = k\left(1 - \cos\left[\frac{2\pi(s - s_{i-1})}{s_i - s_{i-1}}\right]\right), \quad \text{for } i = 1, \cdots, N. \quad (17)$$

Here s_i and s_{i-1} are the parameters corresponding to the starting and ending points of the tow section assuming rotation-free boundary conditions at the two ends along the length, and the amplitude k is computed so that the length of the shorter edge is set equal to the length of the longer one. The integer N in equation (17) represents the number of wrinkling waves along the tow, or also referred here as the mode shape. Note that for $N = 1$ (1st mode shape, or only one wrinkle is assumed) the end points are equal to the start and end of the curve $\boldsymbol{C}(s)$. To calculate the amplitude k of the cosine shape function in equation (17), the equation for the parallel curve at a distance $n = 1$ in equation (15) $\boldsymbol{S_w}(s, 1)$ is computed and inserted into the length calculation using equation (7) (instead of the reference path) with the corresponding start and end points s_i and s_{i-1}, then an iterative method (such as Newton's method) is used to converge for a final value of k such that the total length of the shorter edge is equal to the length of the longer one.

Equation (17) represents the case where the wrinkles have equal wavelength along the analyzed tow section which is a good start for the wrinkling analysis. However, depending on the material properties of the tow, the properties of the tow-substrate interface, and the radius of curvature of the path, an approximate wavelength of the wrinkle can be determined based on mechanics models for tow wrinkling [21,22], or from experimental results [16]. In this case, equation (17) can be modified by taking the first mode shape only ($N = 1$), and then solving for the end-point s_i depending on the chosen wavelength for the wrinkle.

2.6. Simplification for flat plate

To provide a realistic example and verification with actual experiments for tow wrinkling, the previous equations are simplified for a flat surface. The equation for the surface (1) can be represented in three-dimensional space as:

$$\boldsymbol{S}(u, v) = u\hat{i} + v\hat{j}. \quad (18)$$

Computations of the ensuing equations leads to the following relevant equations for the surface:

$$\hat{\boldsymbol{S}}_{\boldsymbol{u}}(u, v) = \hat{i}, \ \hat{\boldsymbol{S}}_{\boldsymbol{v}}(u, v) = \hat{j} \quad (19)$$

$$E = 1, \ F = 0, \ G = 1, \quad \text{and all } \Gamma^i_{jk} = 0. \quad (20)$$

The reference curve $\boldsymbol{C}(s)$ can be simplified and expressed as:

$$\boldsymbol{C}(s) = \boldsymbol{S}(u_c(s), v_c(s)) = u_c(s)\hat{i} + v_c(s)\hat{j}, \quad (21)$$

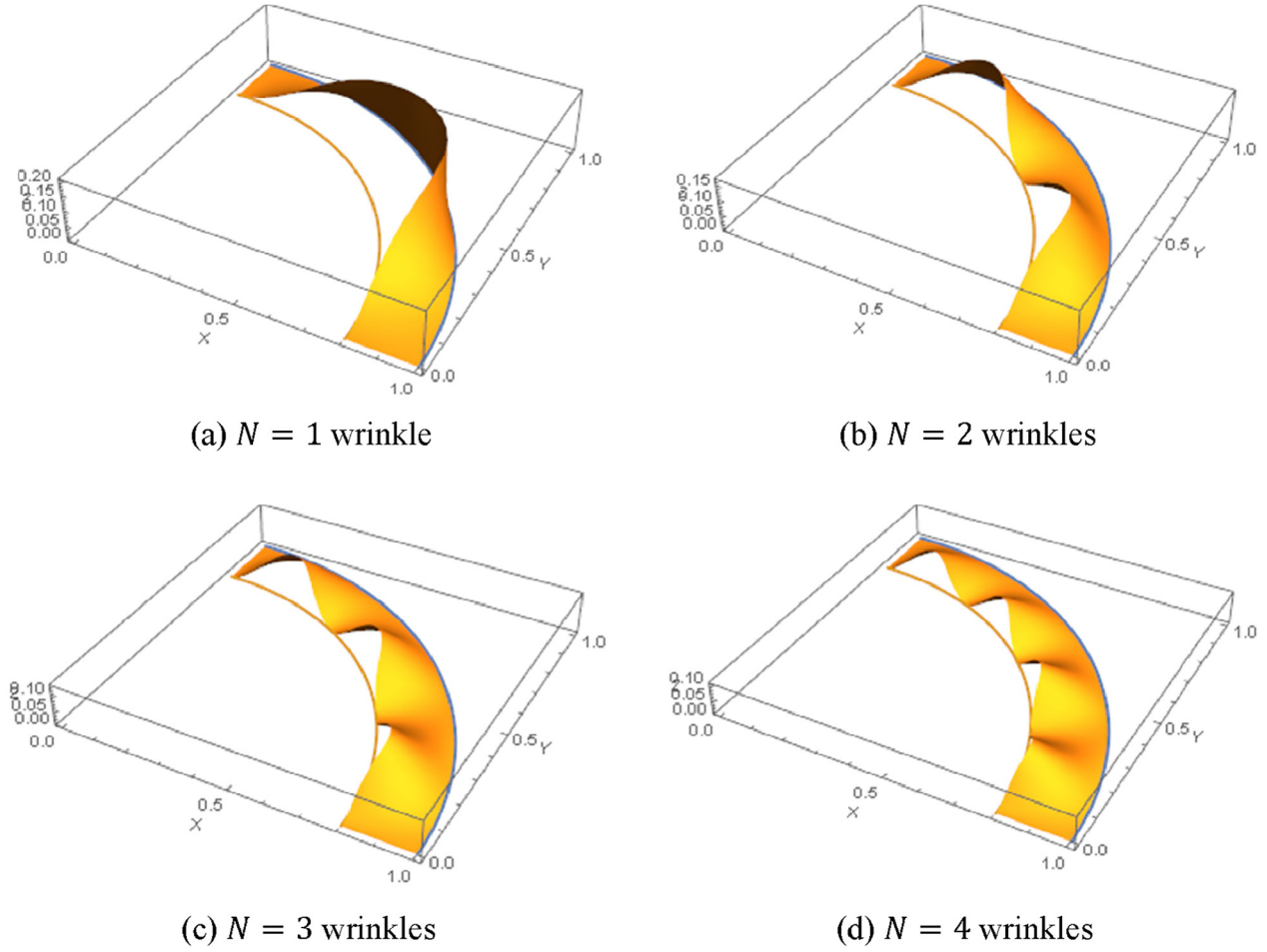

Fig. 7. Deformed tow placed on a circular path: 4 different mode shapes.

with the corresponding normal, tangent, and in-plane normal vectors:

$$\widehat{\boldsymbol{N}}(u, v) = \hat{k} \tag{22}$$

$$\widehat{\boldsymbol{T}}(s) = \hat{u}_c^{'}(s)\hat{i} + \hat{v}_c^{'}(s)\hat{j} \tag{23}$$

$$\widehat{\boldsymbol{B}}(s) = -\hat{v}_c^{'}(s)\hat{i} + \hat{u}_c^{'}(s)\hat{j} \tag{24}$$

with $\hat{u}_c^{'}(s) = u_c^{'}(s)/\|\boldsymbol{C}^{'}(s)\|$, and $\hat{v}_c^{'}(s) = v_c^{'}(s)/\|\boldsymbol{C}^{'}(s)\|$.

Therefore, the parallel edge curve and the tow surface can be stated in a simpler way as:

$$\boldsymbol{C_p}(s): \begin{cases} x_p(s) = u_c(s) - d\hat{v}_c^{'}(s) \\ y_p(s) = v_c(s) + d\hat{u}_c^{'}(s) \end{cases}, \tag{25}$$

$$\boldsymbol{S_{tow}}(s, n) = \boldsymbol{C}(s) + nd\widehat{\boldsymbol{B}}(s), \quad 0 \le s \le L, 0 \le n \le 1, \tag{26}$$

where d is equal to the tow width. The in-plane curvature (simplified version of the geodesic curvature) is calculated from:

$$k_g(s) = \frac{u_c^{'}v_c^{''} - u_c^{''}v_c^{'}}{(u_c^{'2} + v_c^{'2})^{3/2}}. \tag{27}$$

The shape of the wrinkled tow surface $\boldsymbol{S_w}(s, n)$ can be simplified furthermore, and expressed in vector form as:

$$\boldsymbol{S_w}(s, n) = \boldsymbol{C}(s) + nd[\cos(\beta(s))\widehat{\boldsymbol{B}}(s) + \sin(\beta(s))\widehat{\boldsymbol{N}}(s)], \tag{28}$$

or explicitly in terms of the Cartesian three-dimensional space:

$$\boldsymbol{S_w}(s, n): \begin{cases} x_w(s, n) = u_c(s) - nd\hat{v}_c^{'}(s)\cos(\beta(s)) \\ y_w(s, n) = v_c(s) + nd\hat{u}_c^{'}(s)\cos(\beta(s)) \\ z_w(s, n) = nd\sin(\beta(s)) \end{cases}, \tag{29}$$

where $\beta(s)$ is the same cosine shape function for the wrinkle rotation angle as shown earlier in equation (17). The amplitude k of the rotation angle $\beta(s)$ is found using the length calculations for the parallel edge at $n = 1$ and setting it equal to the original path length:

$$\int_{s_{i-1}}^{s_i} \sqrt{\left(\frac{dx_w}{ds}\right)^2 + \left(\frac{dy_w}{ds}\right)^2 + \left(\frac{dz_w}{ds}\right)^2}\, ds = \frac{L}{N} \quad for i = 1, \cdots, N. \tag{30}$$

Lastly, the maximum height the wrinkle will reach occurs at $s_{max} = (s_i - s_{i-1})/2$, resulting in a maximum rotation angle $\beta = 2k$. From equation (29), the amplitude of the wrinkle can be obtained to be:

$$a_w = z_w(s_{max}, 1) = d\sin(2k). \tag{31}$$

3. Modeling test cases

This section demonstrates the implementation of the developed wrinkling equations for paths placed on flat and general surfaces. The first example considers a simple circular path on a flat surface where the effect of number of wrinkles and tow width are investigated while keeping the curvature constant. The second example consists of analyzing the wrinkled shape of a tow placed on a general surface, and the effect of the geodesic curvature on the wrinkling amplitudes. Then, several different layups with fixed-angle reference curves are considered for wrinkling analysis.

3.1. Circular path on a flat surface

To investigate the presented algorithm, a simple constant curvature path is first considered. This path is a circular arc, with a possible parameterization defined as:

$$\boldsymbol{C}(t) = \left\{\cos\left(\frac{\pi}{2}t\right), \sin\left(\frac{\pi}{2}t\right)\right\}, \quad 0 \le t \le 1, \tag{32}$$

where the radius of curvature is constant with a value of 1. A tow width of $w = 0.2$ (non-dimensional units) is first considered, and the parallel path is computed from equation (25), then the wrinkled shaped of the tow in equation (29) is calculated for the first 4 mode shapes ($N = 1, \cdots, 4$) and visualized in Fig. 7.

In Fig. 7, the reference curve $\boldsymbol{C}(t)$ shown in blue remains on the surface while the parallel edge shown in orange will totally lift from the surface and form the wrinkle. Also, it can be directly observed that the amplitude of the wrinkles is affected by the mode shape. With higher number of modes the amplitude of the wrinkles decreases significantly. In addition, within a mode shape the amplitude of the wrinkles for this case is the same; i.e. the three wrinkles in the 3rd mode shape have the same amplitude, similarly for the four wrinkles in the 4th mode shape. This is due to the fact that this circular path has a constant curvature of $k_g = 1$ and constant width $w = 0.2$ leading to a constant differential length.

Relating these results to the actual fiber placement process, higher number of wrinkles can only be achieved by the presence of the adhesion between the tow and the substrate. Hence, with better surface adhesion, the spots where the tow sticks to the surface are increased, therefore the number of wrinkles increases resulting in smaller wrinkle amplitude, and a better layup quality.

Another important geometrical feature to investigate is the effect of tow width on the severity of the wrinkle's formation. To accomplish that, the same reference path $\boldsymbol{C}(t)$ defined in equation (32) is considered for analysis, with different values of the tow width ranging from $w = 0.05$ to $w = 0.3$, resulting in different parallel paths $\boldsymbol{C_p}(t)$. Four of these different tows with different tow width are shown in Fig. 8. To obtain a fair comparison between different tow widths, the same mode shape is applied for all the paths. Visual and numerical interpretations of Fig. 8 shows that increasing the tow width increases the amplitude of the wrinkle.

3.2. Curvilinear paths on a general surface

The first step in the analysis of a 3D towpath is to specify the surface on which the tow is laid down. To do so, the NURBS form of a surface is used since it is compatible with and implemented in most CAD software packages and offers a wide flexibility for the user. A NURBS surface is given by [33]:

$$\boldsymbol{S}(u, v) = \frac{\sum_{i=0}^{n}\sum_{j=0}^{m} N_{i,p}(u) N_{j,q}(v) w_{i,j} P_{i,j}}{\sum_{i=0}^{n}\sum_{j=0}^{m} N_{i,p}(u) N_{j,q}(v) w_{i,j}}. \tag{33}$$

The $P_{i,j}$ are the control points (control net), $w_{i,j}$ are the corresponding weights, $N_{i,p}(u)$ and $N_{j,q}(v)$ are the non-uniform rational B-Splines basis functions of degree p and q, respectively, which are defined over the knot vectors $\boldsymbol{U}$ and $\boldsymbol{V}$ (see [33] for details on NURBS surface parametrization).

To illustrate the calculation presented previously for a general surface, a NURBS surface (shown in gray in Fig. 10) with parameters given in the appendix is considered for analysis along with a path with the following functional form parameters:

$$u_c(t) = \sin\left(\frac{\pi}{2}t\right), \; v_c(t) = t. \tag{34}$$

Therefore, the reference path $\boldsymbol{C}(t)$ has the following equation:

$$\boldsymbol{C}(t) = \boldsymbol{S}(u_c(t), v_c(t)) = \boldsymbol{S}\left(\sin\frac{\pi}{2}t, \, t\right), \quad 0 \le t \le 1. \tag{35}$$

Calculation of the geodesic curvature using equation (12) along the length of this curve on the NURBS surface is shown in Fig. 9. Inspection of the geodesic curvature indicates that the amplitude of the wrinkles will be higher in the first section of the path and lower in the later section. The first four mode shapes generated by implementing the wrinkled shape of the tow from equation (15) are shown in Fig. 10 which agrees with the prediction that the wrinkles are proportional to the geodesic curvature.

Another option that could be used to spatially identify critical location for wrinkling is a geodesic color map of the tows indicating the locations where wrinkles might appear and their severity, as demonstrated in Fig. 11. Four different constant angle layups on the general surface are shown in Fig. 11 where, for visualization purposes, the wrinkled tows are colored with their amplitude normalized by the tow width. Based on the differential length between the two sides of the tow (directly related to the geodesic curvature), the calculations can be used to detect the possible location of the wrinkle. A positive differential length (colored in blue) indicates that wrinkles might appear on the dashed blue side of the represented tow, whereas a negative differential length (colored in yellow–red) indicates that the wrinkles might appear on the solid orange side of the tow. The green region is the best from manufacturing perspective since it is the least portion where wrinkling defect might appear. In addition, the wrinkling equations are applied to the layup at a 45° angle, where the wavelength of the wrinkles are assumed to be equal over the entire layup. A comparison between the geodesic curvature map of this layup (Fig. 11) and the wrinkling map (Fig. 12) shows a good agreement between the two on the location of the critical wrinkles and their direction.

Comparing the different angled layup, it can be clearly noticed that the critical regions of the wrinkles do not depend only on the surface geometry, but also on the chosen paths. For instance, the bottom left corner of the 0° layup is relatively wrinkle free, whereas this area is the most critical for the 45° layup. This implies that a wrinkling analysis is necessary for each layup prior to manufacturing since each layup will behave differently as shown in Fig. 11.

4. Model application to thermoset materials

This section describes the application of the geometrical model to thermoset tows by including information from the literature on mechanics models and from experimental measurements. From the existing mechanics models [21,22] a closed form solution for a critical steering radius can be obtained. If the path is steered above the critical radius, no wrinkles will occur, and all the differential length is absorbed through compressive/tensile strains. When steering below the critical radius, wrinkles will occur with a prescribed wavelength also obtained from these models. The amplitude of the wrinkles can therefore be obtained from the length calculations presented earlier in the geometrical model.

In addition, experimental measurements for the wrinkle wavelength, width, and amplitude for several steering radii is accomplished and detailed in [16]. In a similar way, a critical steering radius can be determined above which no wrinkles will occur. Below that radius, a wrinkle wavelength and width are used to generate the wrinkles, and the amplitudes are calculated using the geometrical model. Lastly, multiple steering examples are used for method validation.

4.1. Wrinkle wavelength from mechanics models

Based on the mechanics available in the literature [20–22], the wrinkle wavelength for a given radius of curvature and material properties can be obtained from closed form solutions. The deformed shape of the tow can therefore be generated for the given wavelength

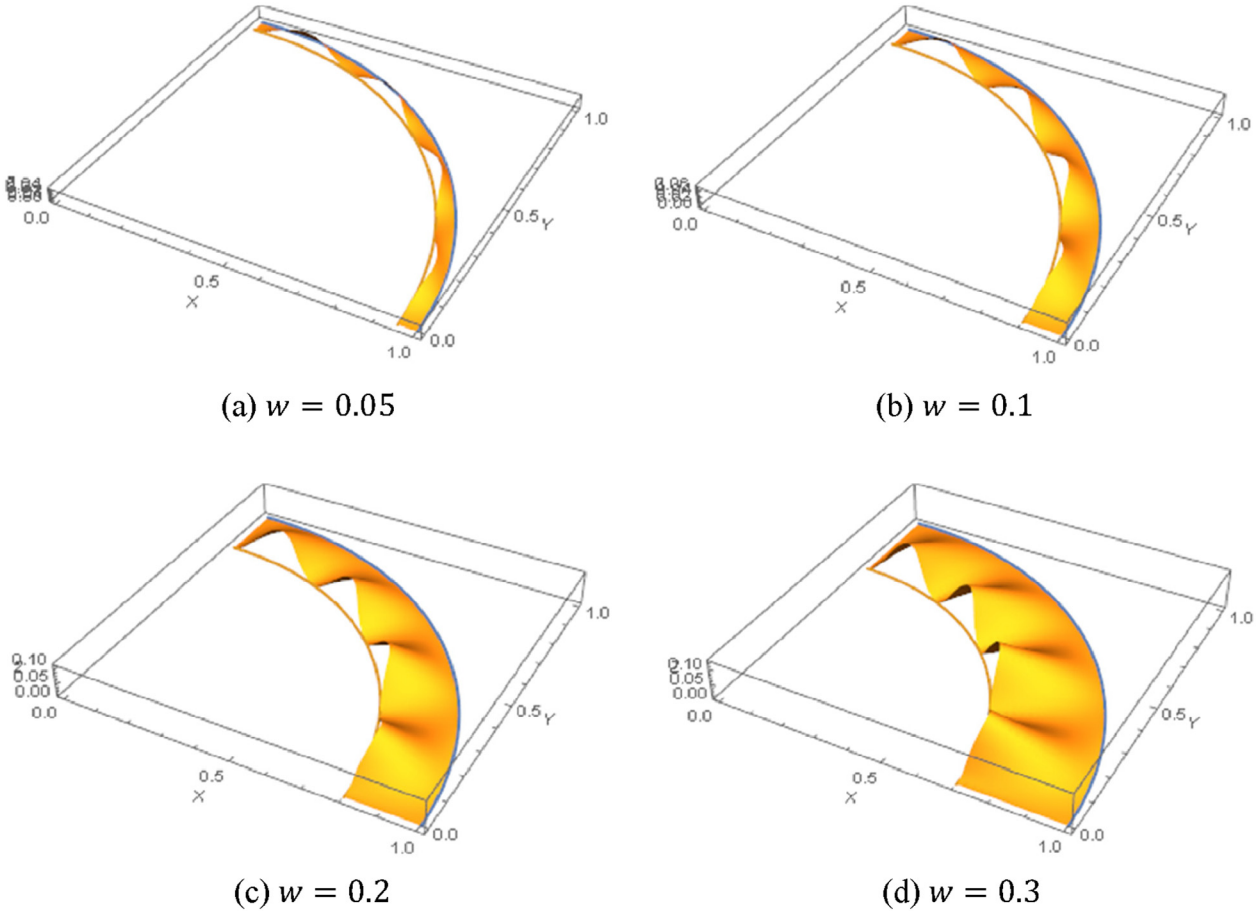

Fig. 8. Effect of tow width on the wrinkles' amplitude.

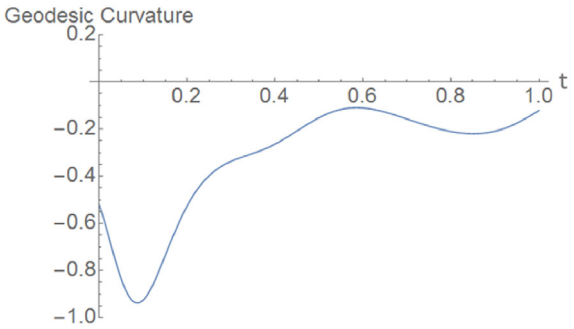

Fig. 9. Geodesic curvature of the reference path on the NURBS surface.

using a cosine function consistent with the assumed shape function in the Raleigh-Ritz method used in the literature. As a result, the wrinkle wavelength L can be obtained by solving the following biquadratic equation [22]:

$$\mathscr{A}L^4 + \mathscr{B}L^2 + \mathscr{C} = 0, \tag{36}$$

with:

$$\mathscr{A} = 90D_{22}\left(\frac{1}{\pi m b^2}\right)^2 + \frac{9}{2}k\left(\frac{1}{\pi m}\right)^2 + 30G\left(\frac{1}{\pi m b}\right)^2, \tag{37}$$

$$\mathscr{B} = 160D_{66}\left(\frac{1}{b}\right)^2 - 40D_{12}\left(\frac{1}{b}\right)^2 - (6-\alpha)\left(\frac{E_1 hb}{\alpha R}\right) + 6G, \tag{38}$$

$$\mathscr{C} = 24D_{11}(\pi m)^2. \tag{39}$$

The D_{ij} terms in equations (37)–(39) are the components of the bending stiffness matrix of a composite plate, which for a single layer, can be expressed as:

$$D_{11} = \frac{E_1 h^3}{12(1-\nu_{12}\nu_{21})}, \quad D_{12} = \nu_{21}D_{11}, \quad D_{22} = \frac{E_2}{E_1}D_{11}, \quad D_{66} = \frac{G_{12}h^3}{12}. \tag{40}$$

The remaining parameters required to solve equation (36) are defined as follows: k and G are the normal and shear stiffnesses of the elastic foundation, b and h are the tow width and thickness respectively, m is the number of wrinkle wavelength (m is taken to be equal to 1 for an isolated wrinkle in these models), α is the load non-uniformity coefficient ($\alpha = 0$ corresponds to uniform compression, $\alpha = 1$ corresponds to a load decaying from the inner tow edge to the outer one, and $\alpha = 2$ corresponds to pure bending). Note that equation (36) admits a real solution only when $\mathscr{B}^2 \geq 4\mathscr{A}\mathscr{C}$.

Assuming that the material properties of the tow and substrate can be obtained through accurate experimental measurements, and that these properties are consistent along the length of the tow-path, the only remaining variable affecting the wavelength of the wrinkles would be the path curvature R. For the material properties of an uncured tow obtained from the literature [20,22,23] and presented in Table 1, the relationship between the wavelength and the steering radius is plotted based on the solution of equation (36) and shown in Fig. 13. Note that only the positive increasing root is chosen from the solution of (36) and shown in Fig. 13 consistent with the literature [22]. It can be observed that the relationship between the wavelength and the steering radius is quasi-linear for a significant range of the steering radius. In addition, the closed form solution for the critical steering radius provided in [22] results in $R_{critical} = 1303mm$ for the provided parameters in Table 1. For a steering radius above this value, the roots for (35) become complex numbers, and wrinkles do not occur along the path.

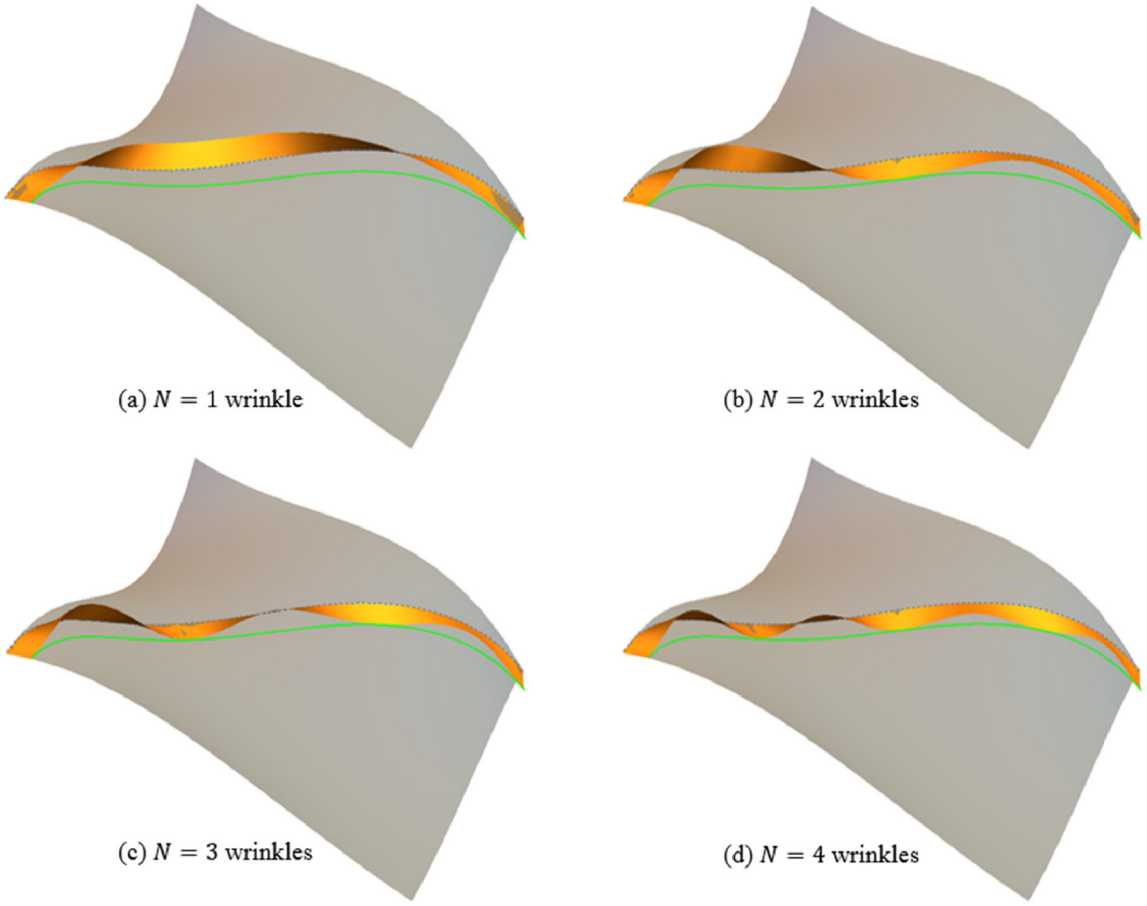

Fig. 10. First 4 mode shapes of a tow placed on a NURBS surface.

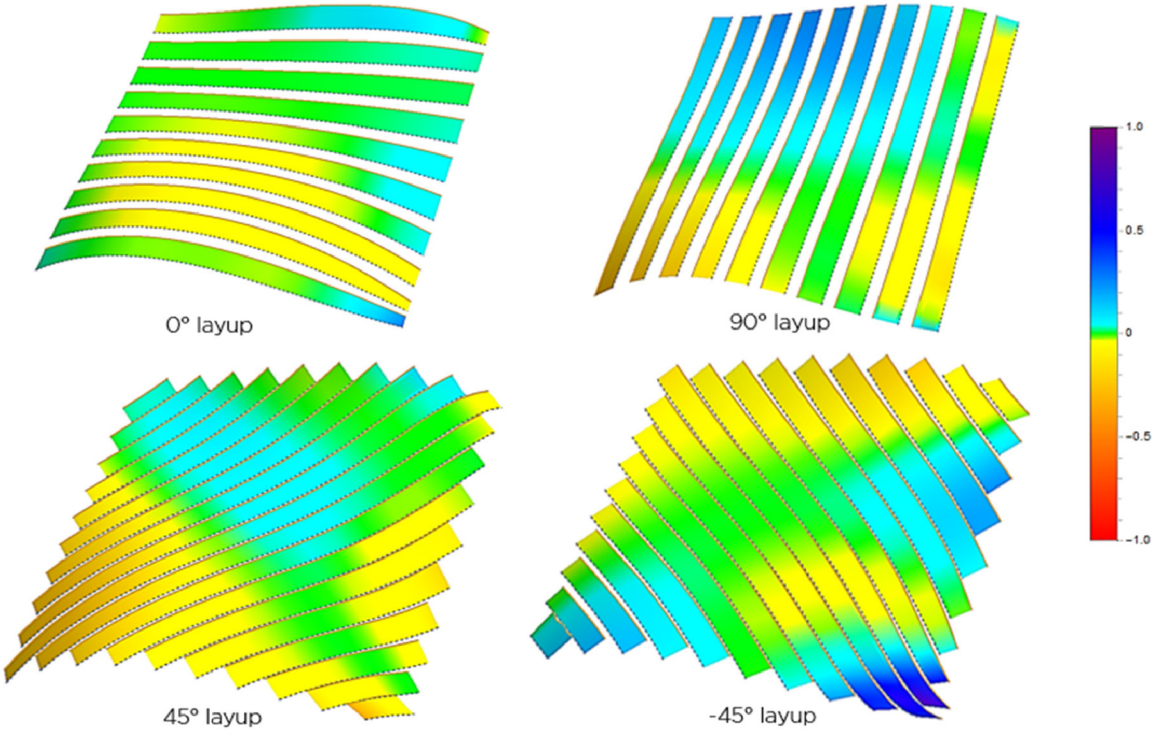

Fig. 11. Geodesic curvature color map for different layup on the NURBS surface.

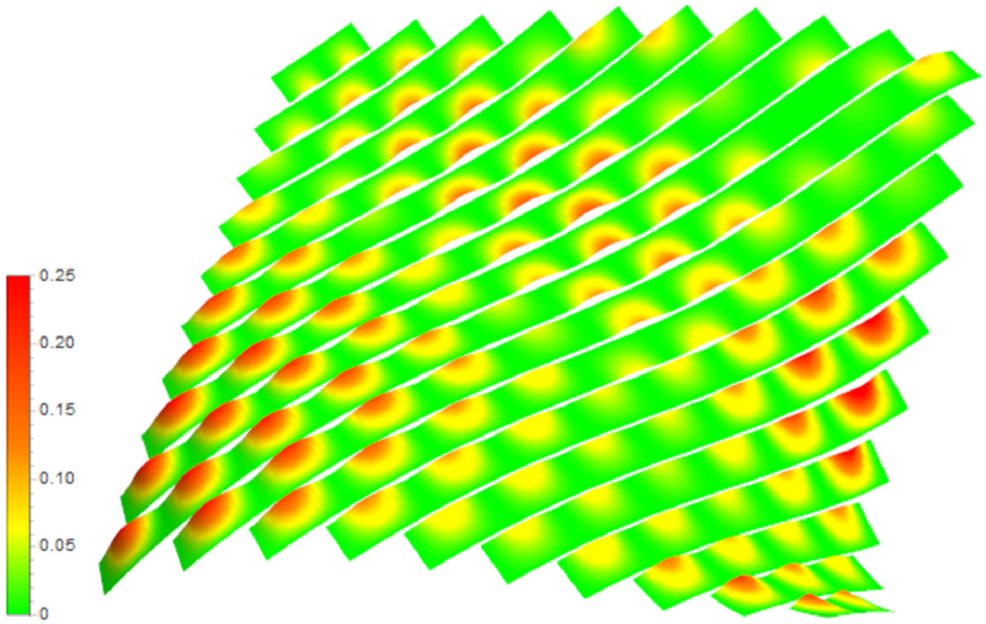

Fig. 12. Wrinkling map for the 45° layup on the NURBS surface.

The algorithm for the geometrical model based on mechanics information is described as follows. For a given path, the steering radius (inverse of curvature (27)) should be captured first. For regions where the steering radius is above the critical steering radius, no wrinkles occur, and the wrinkled tow surface remains the same as the original tow surface which can be accomplished by setting k, the amplitude of the rotation angle in (17) to zero. For areas where the radius of curvature is below the critical one, the corresponding boundaries of the wrinkles can be obtained successively by relating the radius to the wavelength obtained from the mechanics model (Fig. 13). Once these boundaries are determined, the wrinkled surface of the tow can be obtained by carrying the length calculations as described earlier in the geometrical model. Therefore, as the analysis progresses along the length of the path, local wrinkles can be generated with different sizes depending on the path curvature and having the other material properties fixed. This approach can be generalized and applied for curves on general surfaces by taking the geodesic curvature of the path (12) to be the relevant parameter for the wrinkle formation since it is responsible for the tow bending in a plane tangent to the surface at the given location. The geodesic curvature is then compared to the critical curvature from the mechanics model and the algorithm proceeds similarly to the flat case.

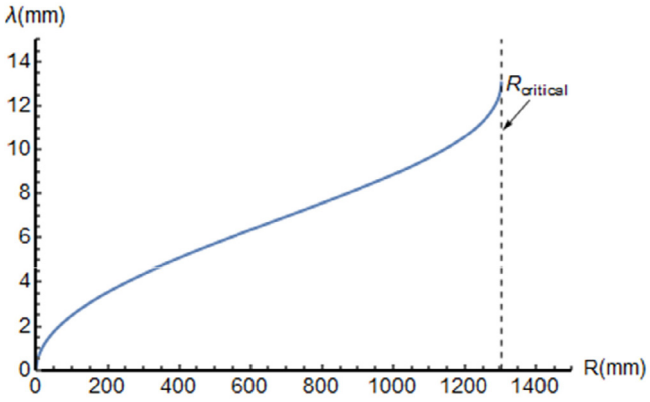

Fig. 13. Wrinkle wavelength as a function of steering radius based on mechanics model [22].

4.2. Wrinkle wavelength and width from experimental results

Another approach to improve the geometrical model is to include information from steering experiments. The key difference between the pure geometrical model, its improvement based on mechanics model and the presented model in this section is that the wrinkle is characterized not only by its wavelength, but also by its width. The wrinkle wavelength λ_w is defined as the distance between two adjacent peaks along a path, and the wrinkle width l_w as the total length the tow is separated from the substrate. In general, the wrinkle width is smaller than the wavelength. By identifying these two key parameters, a more

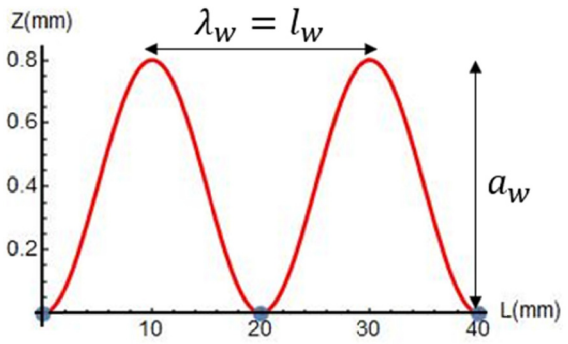

Fig. 14. Shape of the wrinkle used in geometrical model.

Table 1
Material properties and geometry of uncured tow obtained from [20,22,23].

E1 (GPa)	E2 (MPa)	G12 (MPa)	ν_{12}	ν_{21}	h (mm)	b (mm)	α	G (N/m)	k (N/m^3)
31	0.046	3.025	0.2	0.02	0.2	6.35	2	605	2.65×10^8

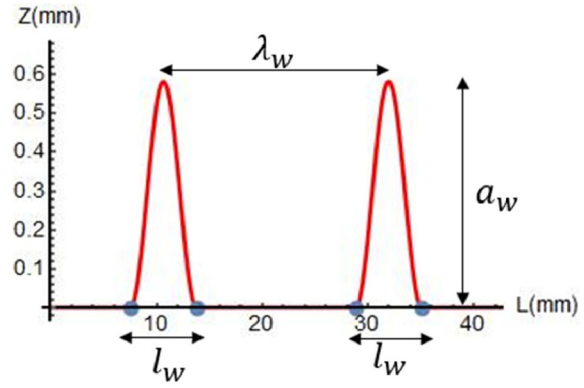

Fig. 15. Shape of the wrinkle used in the improved model based on experimental data.

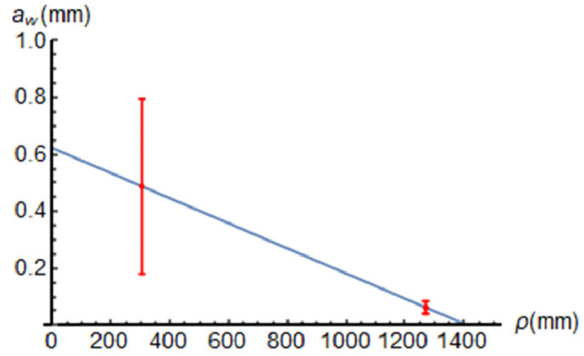

Fig. 16. Measured wrinkle amplitude as a function of steering radius.

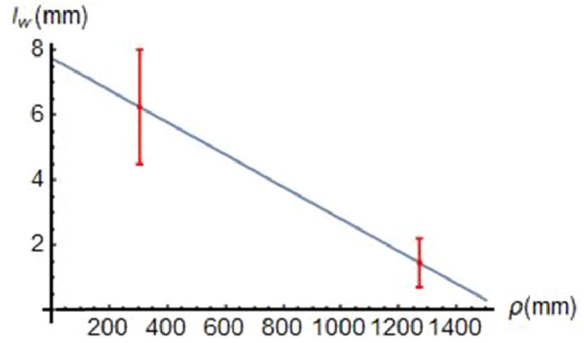

Fig. 17. Measured wrinkle width as a function of steering radius.

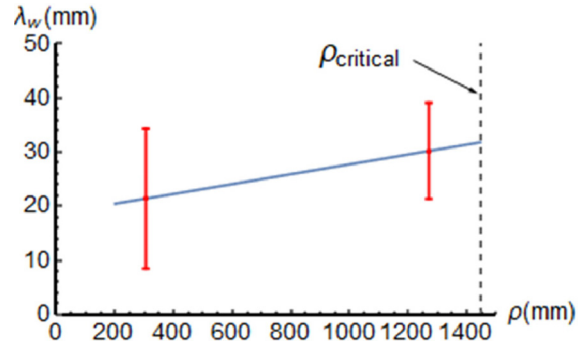

Fig. 18. Measured wrinkle wavelength as a function of steering radius.

accurate representation of the wrinkles can be achieved especially for thermoset materials where significant areas of the tow remain adhered to the substrate and other deformation mechanisms occur. The representations for the shape of the wrinkles including these parameters as well as the original assumption are shown below in Figs. 14 and 15.

Several experimental trials are carried out, and measurements of wrinkles' wavelengths, amplitudes, and widths are obtained by the authors using stereo DIC for different radii of curvature. The detailed methodology and results can be found in [16]. For the purpose of this section, these quantities are plotted against the steering radius and shown in Figs. 16, 17, and 18. Linear interpolation functions are used to fit the experimental data points. These functions are extrapolated to intersect with the radius axes for the amplitude and width hence resulting in a critical steering radius. The obtained critical radii are 1410 mm and 1482 mm for the amplitude and width respectively. Hence an average of 1446 mm is used as a critical radius for wrinkles to occur for the thermoset material and the set of process parameters used in [16].

Based on the critical steering radius deduced from the experimental measurements, the geometrical model identifies the critical areas where the corresponding critical curvature is exceeded and generates wrinkles. The shape of the wrinkle however is different for this case: for a given wavelength, some areas along the length remain bonded to the substrate due to other deformation mechanisms that occur, and a cosine function is only applied to the width of the wrinkle as shown in Fig. 15. It is assumed that the wrinkle's width is centered along the wavelength, and two equal regions of bonded material is assumed from each side. Based on these assumptions, the boundaries where the wrinkle separates from the substrate can be determined, and the length calculation can be carried to determine the final shape and amplitude of the wrinkle. As the analysis progresses along the length of the tow-path, different wrinkles wavelength, width and amplitudes are generated based on the curvature. This approach creates a more realistic case where out-of-plane wrinkles are not the only deformation mechanisms that occur. This approach can also be extrapolated to curves on general surfaces by taking the geodesic curvature as the key parameter for wrinkle formation as described in the previous section.

4.3. Steered paths examples

In this section, the improved model based on experimental results from thermoset material is applied for several examples. In a first step, the calculations of the wrinkle shape and amplitude from the geometrical model is compared to the original geometrical model and to the actual shape measurement obtained from DIC. To do so, a 6.35 mm wide tow is place on a constant curvature path steered at 305 mm radius is considered for analysis. For a constant curvature path, the wrinkle's wavelength and width are constant along the path and are equal to 21.43 mm and 8.03 mm respectively [16]. A comparison between the prediction of the original geometrical model and the improved one for the same wavelength is shown in Fig. 19. It can be observed that the improved model gives a better approximation of tow wrinkling for thermoset materials by considering additional bonded areas to the substrate consistent with the results observed during experiments reported in [16]. In addition, the out-of-plane displacement extracted at 1 mm above the bottom edge of the tow is show in Fig. 20 for both experimental measurements and model prediction. It can be observed that the computed amplitude of the wrinkles from geometry given the wavelength and width of the wrinkles falls within the range of the measured amplitude from experimental results. The difference between the model prediction and the measurement can be related to the variability of the wrinkles wavelength and width during the process as reported in [16], however, in the model, only the averages of these measurements are taken into considerations.

Another example containing variable curvature paths is considered for analysis. It consists of multiple sinusoidal path with varying amplitudes. This family of curves is defined by:

$$\boldsymbol{C}(t) = \{300\pi t,\ a_m \sin(2\pi t) + c,\ 0\}, \quad 0 \le t \le 1, \tag{41}$$

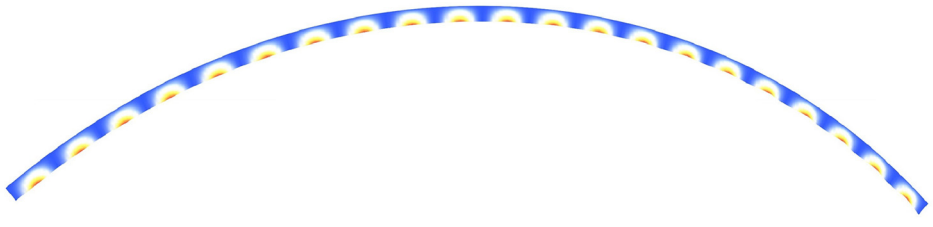

(a) Geometrical model with 21.43 mm wavelength

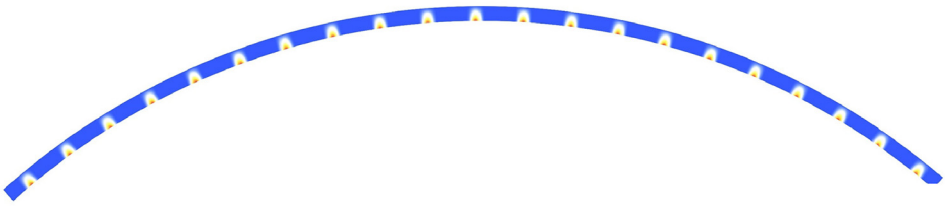

(b) Improved model from experiment

Fig. 19. Comparison between the geometrical model and the improved model from experimental data for a steering radius of 305 mm.

where a_m is the amplitude of the sine waves ranging from 10 mm to 80 mm with an increment of 10 mm, and c is a constant for translation along the y-axis to avoid overlapping paths. The tow width is taken at 6.35 mm consistently with the experimental results. The wrinkles patterns for these paths obtained from the improved model based on the experimental data are shown in Fig. 21. It can be observed that for the path with $a_m = 10mm$ no wrinkles appear along the path. A further examination of the curvature reveals that the minimum steering radius for this path is 2250 mm which is above the critical radius obtained from the experiments. As the amplitude of the sine waves increases, the curvature of the paths increases as well, and wrinkles start to appear along the tow. In addition, with higher curvature, the wrinkles become wider, larger, and closer to each other consistent with the trends observed in the experiments.

5. Discussions

Several defects might arise during manufacturing of fiber reinforced composite structures using the Automated Fiber Placement process. One of the predominant defects is tow wrinkling, which is studied based on the mismatch in length between the tow-path on the placement surface and the actual length of the tow delivered from the machine head. In the presented work, geometrical parameters affecting tow wrinkling are investigated along with an experimental measurement regarding the wrinkle's wavelength. A worst-case scenario is assumed where all the differential length is absorbed by wrinkles formation in the out-of-plane direction when steered or placed on a general curved surface.

The implementation of the wrinkling governing equations to several examples is presented. For the case of a constant curvature circular path placed on a flat surface effects of the tow width and wrinkle numbers is studied. Numerical results show that increasing the tow width will lead to higher amplitude of wrinkles. However, increasing the number of wrinkles within a prescribed path results in a lower wrinkling amplitude. Higher number of wrinkles can be achieved in the presence of good adhesion between the tow and the substrate. For the case of paths on a general surface, an arbitrary path on a quasi-random NURBS surface is analyzed. The results show that the wrinkles amplitude is

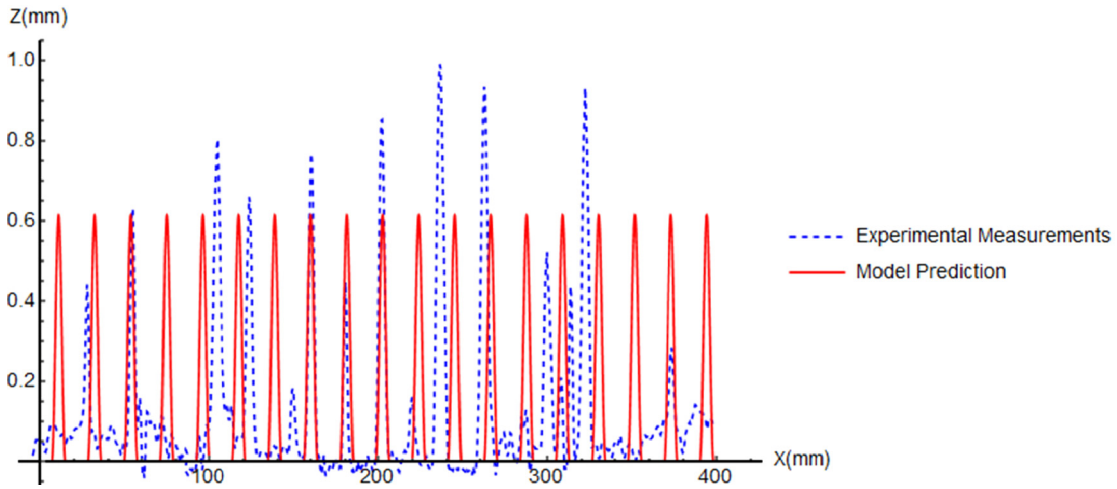

Fig. 20. Model prediction vs experimental measurements reproduced from [16] of the out-of-plane displacements for a path steered at 305 mm radius at a line 1 mm above the bottom edge.

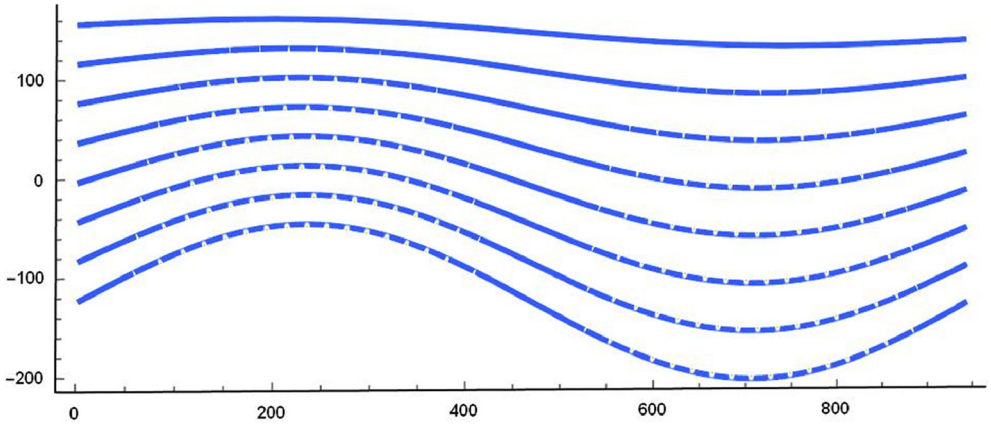

Fig. 21. Wrinkle prediction for a layup of sinusoidal paths with variable amplitudes (units in mm).

proportional to the geodesic curvature of the path. In addition, four different constant angle layups ($\pm$ 45°, 0°, and 90°) on the same NURBS surface are analyzed and results are shown in colored maps indicating possible regions of wrinkling. It is concluded that for the same placement surface, different angled layups have different critical regions for wrinkling.

The model application to thermoset material is discussed in Section 4. The wrinkle's wavelength can be approximated using closed form solutions from existing mechanics model in the literature. To be able to apply these models adequately, several elaborate material characterization tests are needed for the uncured tow to determine necessary parameters such as tackiness with the substrate, longitudinal, transverse and shear stiffnesses. In the present paper the wrinkle's width and wavelength are determined from experimental measurements of wrinkles that appear on constant curvature paths placed by AFP machines. Comparison of the measured amplitudes with those based on the calculation of the geometrical model showed a good agreement.

Identifying critical regions within a layup can help the designer and the manufacturer to adjust the process parameters such as the speed, temperature, tension, and compaction pressure to alleviate the wrinkling formation. In addition, knowing the amplitude of the wrinkles, a threshold can be set where small wrinkles can be considered as not a major defect and therefore neglected during the layup, especially when successive layers will compress them downwards, thus pushing the steering limits of AFP even further.

6. Data availability

The raw/processed data required to reproduce these findings cannot be shared at this time as the data also forms part of an ongoing study.

CRediT authorship contribution statement

Roudy Wehbe: Methodology, Software, Validation, Writing - original draft, Writing - review & editing, Visualization. **Brian Tatting:** Conceptualization, Methodology, Validation. **Sreehari Rajan:** Validation, Investigation. **Ramy Harik:** Project administration, Supervision. **Michael Sutton:** Validation, Investigation, Supervision. **Zafer Gürdal:** Conceptualization, Funding acquisition, Supervision.

Declaration of Competing Interest

The authors declare that they have no known competing financial interests or personal relationships that could have appeared to influence the work reported in this paper.

Acknowledgements

The authors at the McNAIR Center would like to thank The Boeing Company for their support of this work. This research was performed under contract SSOW-BRT-W0915-0006 through the University of South Carolina and has been released for publication by The Boeing Company. The technical support and assistance of the McNair technical staff during operation of the AFP is also greatly appreciated. Finally, the support of Ms. Eileen Miller, Boeing Research and Technology in Charleston, SC, is gratefully acknowledged.

Appendix

Γ^i_{jk} are the Christoffel symbols of the surface $\boldsymbol{S}$ given in the appendix. by:

$$\Gamma^1_{11} = \frac{GE_u - 2FF_u + FE_v}{2(EG - F^2)}, \tag{42}$$

$$\Gamma^2_{11} = \frac{2EF_u - EE_v - FE_u}{2(EG - F^2)}, \tag{43}$$

$$\Gamma^1_{12} = \frac{GE_v - FG_u}{2(EG - F^2)}, \tag{44}$$

$$\Gamma^2_{12} = \frac{EG_u - FE_v}{2(EG - F^2)}, \tag{45}$$

$$\Gamma^1_{22} = \frac{2GF_v - GG_u - FG_v}{2(EG - F^2)}, \tag{46}$$

$$\Gamma_{22}^2 = \frac{EG_v - 2FF_v + FG_u}{2(EG - F^2)}. \tag{47}$$

The following parameters are used to generate the NURBS surface:

$$P_{i,j} = \begin{Bmatrix} \{\{1, 1, -0.643\}, \{1, 2, -0.404\}, \{1, 3, -0.795\}, \{1, 4, -0.513\}\}, \\ \{\{2, 1, 0.692\}, \{2, 2, 0.281\}, \{2, 3, -0.458\}, \{2, 4, -0.14\}\}, \\ \{\{3, 1, 0.085\}, \{3, 2, 0.986\}, \{3, 3, -0.693\}, \{3, 4, 0.678\}\}, \\ \{\{4, 1, 0.502\}, \{4, 2, -0.999\}, \{4, 3, 0.804\}, \{4, 4, 0.475\}\} \end{Bmatrix} \tag{48}$$

$$w_{ij} = \{\{1, 1, 1, 1\}, \{1, 1, 1, 1\}, \{1, 1, 1, 1\}, \{1, 1, 1, 1\}\} \tag{49}$$

$$\boldsymbol{U} = \boldsymbol{V} = \{0, 0, 0, 0, 1, 1, 1, 1\} \tag{50}$$

$$p = q = 3 \tag{51}$$

Appendix A. Supplementary data

Supplementary data to this article can be found online at https://doi.org/10.1016/j.compstruct.2020.112394.

References

[1] Lukaszewicz DHJA, Ward C, Potter KD. The engineering aspects of automated prepreg layup: history, present and future. Compos Part B Eng 2012;43:997–1009. https://doi.org/10.1016/j.compositesb.2011.12.003.

[2] Debout P, Chanal H, Duc E. Tool path smoothing of a redundant machine: application to automated fiber placement. CAD Comput Aided Des 2011;43:122–32. https://doi.org/10.1016/j.cad.2010.09.011.

[3] Rajan S, Sutton MA, Wehbe R, Tatting B, Gurdal Z, Kidane A. Measured surface deformation and strains in thin thermoplastic prepreg tapes steered along curved paths without adhesion using StereoDIC. Exp Mech 2019;59:531–47. https://doi.org/10.1007/s11340-019-00478-3.

[4] Harik R, Saidy C, Williams SJ, Gurdal Z, Grimsley B. Automated fiber placement defect identity cards: cause, anticipation, existence, significance, and progression. Long Beach, California: Sampe; 2018.

[5] Oromiehie E, Prusty BG, Compston P, Rajan G. Automated fibre placement based composite structures: review on the defects, impacts and inspections techniques. Compos Struct 2019;224:110987https://doi.org/10.1016/j.compstruct.2019.110987.

[6] Sacco C, Radwan AB, Harik R, Van Tooren M. Automated fiber placement defects: automated inspection and characterization. SAMPE 2018 Conf. Proceeding, Long Beach, California. 2018.

[7] Rousseau G, Wehbe R, Halbritter J, Harik R. Automated fiber placement path planning: a state-of-the-art review. Comput Aided Des Appl 2018;16:172–203. https://doi.org/10.14733/cadaps.2019.172-203.

[8] Li J, Xu W, Cheng Z, Xu K, Klein R. Lightweight wrinkle synthesis for 3D facial modeling and animation. CAD Comput Aided Des 2015;58:117–22. https://doi.org/10.1016/j.cad.2014.08.016.

[9] Choi KJ, Ko HS. Research problems in clothing simulation. CAD Comput Aided Des 2005;37:585–92. https://doi.org/10.1016/j.cad.2004.11.002.

[10] Eran S, Marder M, Swinney HL. Leaves, flowers and garbage bags: making waves. Am Sci 2004;92:254–61. https://doi.org/10.1511/2004.47.932.

[11] Cerda E, Mahadevan L. Geometry and physics of wrinkling. Phys Rev Lett 2003;90:074302https://doi.org/10.1103/PhysRevLett.90.074302.

[12] Jing F, Joneja A, Tang K. Modeling wrinkles on smooth surfaces for footwear design. CAD Comput Aided Des 2004;1:311–9. https://doi.org/10.1080/16864360.2004.10738272.

[13] Wehbe R. Modeling of tow wrinkling in automated fiber placement based on geometrical considerations. University of South Carolina; 2017.

[14] Wehbe RY, Harik R, Gurdal Z. In-plane tow deformations due to steering in automated fiber placement. AIAA Scitech 2019 Forum. Reston, Virginia: American Institute of Aeronautics and Astronautics; 2019. https://doi.org/10.2514/6.2019-1271.

[15] Wehbe R, Tatting B, Gürdal Z, Harik R. Fiber Tow deformations during layup of steered paths using automated fiber placement process. SAMPE 2019 - Charlotte, NC, SAMPE; 2019. https://doi.org/10.33599/nasampe/s.19.1591.

[16] Rajan S, Sutton MA, Wehbe R, Tatting B, Gürdal Z, Kidane A, et al. Experimental investigation of prepreg slit tape wrinkling during automated fiber placement process using StereoDIC. Compos Part B Eng 2019;160:546–57. https://doi.org/10.1016/j.compositesb.2018.12.017.

[17] Bakhshi N, Hojjati M. An experimental and simulative study on the defects appeared during tow steering in automated fiber placement. Compos Part A Appl Sci Manuf 2018;113:122–31. https://doi.org/10.1016/j.compositesa.2018.07.031.

[18] Zhao C, Xiao J, Huang W, Huang X, Gu S. Layup quality evaluation of fiber trajectory based on prepreg tow deformability for automated fiber placement. J Reinf Plast Compos 2016;35:1576–85. https://doi.org/10.1177/0731684416659933.

[19] Smith R, Qureshi Z, Scaife R, El-Dessouky H. Limitations of processing carbon fibre reinforced plastic/polymer material using automated fibre placement technology. J Reinf Plast Compos 2016;35:1527–42. https://doi.org/10.1177/0731684416659544.

[20] Beakou A, Cano M, Le Cam JB, Verney V. Modelling slit tape buckling during automated prepreg manufacturing: a local approach. Compos Struct 2011;93:2628–35. https://doi.org/10.1016/j.compstruct.2011.04.030.

[21] Matveev MY, Schubel PJ, Long AC, Jones IA. Understanding the buckling behaviour of steered tows in Automated Dry Fibre Placement (ADFP). Compos Part A Appl Sci Manuf 2016;90:451–6. https://doi.org/10.1016/j.compositesa.2016.08.014.

[22] Belhaj M, Hojjati M. Wrinkle formation during steering in automated fiber placement: modeling and experimental verification. J Reinf Plast Compos 2018;37:396–409. https://doi.org/10.1177/0731684417752872.

[23] Bakhshi N, Hojjati M. Time-dependent wrinkle formation during tow steering in automated fiber placement. Compos Part B Eng 2019;165:586–93. https://doi.org/10.1016/j.compositesb.2019.02.034.

[24] Blom AW, Tatting BF, Hol JMAM, Gürdal Z. Fiber path definitions for elastically tailored conical shells. Compos Part B Eng 2009;40:77–84. https://doi.org/10.1016/j.compositesb.2008.03.011.

[25] Lopes CS, Gürdal Z, Camanho PP. Variable-stiffness composite panels: Buckling and first-ply failure improvements over straight-fibre laminates. Comput Struct 2008;86:897–907. https://doi.org/10.1016/j.compstruc.2007.04.016.

[26] Blom AW, Abdalla MM, Gürdal Z. Optimization of course locations in fiber-placed panels for general fiber angle distributions. Compos Sci Technol 2010;70:564–70. https://doi.org/10.1016/j.compscitech.2009.12.003.

[27] Gray A. Modern differential geometry of curves and surfaces with mathematica. second ed. CRC Press LLC; 1998.

[28] Schueler K, Miller J, Hale R. Approximate geometric methods in application to the modeling of fiber placed composite structures. J Comput Inf Sci Eng 2004;4:251. https://doi.org/10.1115/1.1736685.

[29] Yan L, Chen ZC, Shi Y, Mo R. An accurate approach to roller path generation for robotic fibre placement of free-form surface composites. Robot Comput Integr Manuf 2014;30:277–86. https://doi.org/10.1016/j.rcim.2013.10.007.

[30] Shirinzadeh B, Cassidy G, Oetomo D, Alici G, Ang MH. Trajectory generation for open-contoured structures in robotic fibre placement. Robot Comput Integr Manuf 2007;23:380–94. https://doi.org/10.1016/j.rcim.2006.04.006.

[31] Gálvez A, Iglesias A, Puig-Pey J. Computing parallel curves on parametric surfaces. Appl Math Model 2014;38:2398–413. https://doi.org/10.1016/j.apm.2013.10.042.

[32] Murray RM, Li Z, Sastry SS. A mathematical introduction to robotic manipulation. CRC Press; 2017. https://doi.org/10.1201/9781315136370.

[33] Piegl L, Tiller W. The NURBS book. second ed. Second Edi: Springer; 1997.